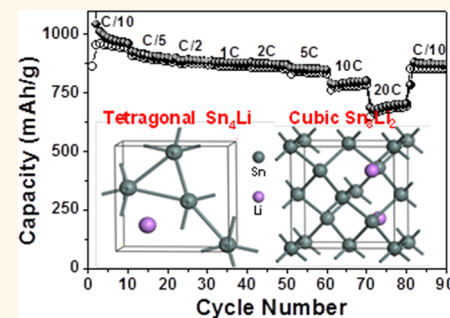


# Phase Evolution of Tin Nanocrystals in Lithium Ion Batteries

Hyung Soon Im,<sup>†</sup> Yong Jae Cho,<sup>†</sup> Young Rok Lim,<sup>†</sup> Chan Su Jung,<sup>†</sup> Dong Myung Jang,<sup>†</sup> Jeunghee Park,<sup>†,\*</sup> Fazel Shoaiei,<sup>‡</sup> and Hong Seok Kang<sup>§,\*</sup>

<sup>†</sup>Department of Chemistry, Korea University, Jochiwon 339-700, Korea, <sup>‡</sup>Department of Chemistry and Bioactive Material Sciences and Research Institute of Physics and Chemistry, Jeonbuk National University, Jeonju, Chonbuk 561-756, Korea, and <sup>§</sup>Department of Nano and Advanced Materials, College of Engineering, Jeonju University, Jeonju, Chonbuk 560-759, Korea

**ABSTRACT** Sn-based nanostructures have emerged as promising alternative materials for commercial lithium–graphite anodes in lithium ion batteries (LIBs). However, there is limited information on their phase evolution during the discharge/charge cycles. In the present work, we comparatively investigated how the phases of Sn, tin sulfide (SnS), and tin oxide (SnO<sub>2</sub>) nanocrystals (NCs) changed during repeated lithiation/delithiation processes. All NCs were synthesized by a convenient gas-phase photolysis of tetramethyl tin. They showed excellent cycling performance with reversible capacities of 700 mAh/g for Sn, 880 mAh/g for SnS, and 540 mAh/g for SnO<sub>2</sub> after 70 cycles. Tetragonal-phase Sn ( $\beta$ -Sn) was produced upon lithiation of SnS and SnO<sub>2</sub> NCs. Remarkably, a cubic phase of diamond-type Sn ( $\alpha$ -Sn) coexisting with  $\beta$ -Sn was produced by lithiation for all NCs. As the cycle number increased,  $\alpha$ -Sn became the dominant phase. First-principles calculations of the Li intercalation energy of  $\alpha$ -Sn (Sn<sub>8</sub>) and  $\beta$ -Sn (Sn<sub>4</sub>) indicate that Sn<sub>4</sub>Li<sub>x</sub> ( $x \leq 3$ ) is thermodynamically more stable than Sn<sub>8</sub>Li<sub>x</sub> ( $x \leq 6$ ) when both have the same composition.  $\alpha$ -Sn maintains its crystalline form, while  $\beta$ -Sn becomes amorphous upon lithiation. Based on these results, we suggest that once  $\alpha$ -Sn is produced, it can retain its crystallinity over the repeated cycles, contributing to the excellent cycling performance.



**KEYWORDS:** tin nanocrystals · phase evolution · tetragonal phase · cubic phase · lithium ion batteries · first-principles calculations · lithium intercalation energy

As with other group IV elements, Sn is of interest as a promising alternative material for commercial lithium–graphite anodes in lithium ion batteries (LIBs).<sup>1–3</sup> The bulk phase is known to have a higher theoretical capacity, 990 mAh/g, than that of graphite (370 mAh/g), owing to Li alloy formation (*i.e.*, Li<sub>4.4</sub>Sn). Sn is also less toxic and less expensive than other candidates. However, huge volume changes (up to 300%) during Li insertion and extraction limit the energy capacity and cycle lifetime of LIBs. It is being increasingly recognized that amorphization occurring during lithiation could have a significant impact on stress generation and fracture. Nanostructures with diverse morphologies have been widely developed in order to minimize the volume change and dissipate the mechanical stress because of their increased surface/volume ratios.<sup>4–13</sup> The nanoscale size also promotes faster diffusion of Li<sup>+</sup> ions (by reducing the diffusion length within the material), and therefore, a higher charging

rate is possible. Another strategy for mitigating the stress due to volume change is to use carbon (C) coating (or hosting) or oxide/sulfide compounds, in which they are able to provide a buffer matrix with high Li<sup>+</sup> ion conductivity.<sup>4–32</sup> It is known that tin sulfide (SnS or SnS<sub>2</sub>) and tin oxide (SnO<sub>2</sub>) are irreversibly converted to Sn in the first cycle of use: SnS + 2Li<sup>+</sup> + 2e<sup>−</sup> → Sn + Li<sub>2</sub>S; SnO<sub>2</sub> + 4Li<sup>+</sup> + 4e<sup>−</sup> → Sn + 2Li<sub>2</sub>O. Subsequently, Sn can efficiently store and release Li ions inside amorphous Li<sub>2</sub>S (or Li<sub>2</sub>O) buffer matrix, according to the reversible Li–Sn alloying/dealloying reaction expressed by Sn + xLi<sup>+</sup> + xe<sup>−</sup> ↔ Li<sub>x</sub>Sn (0 ≤ x ≤ 4.4).

Herein, we investigated the structure and phase evolution underlying the lithiation/delithiation processes of Sn-based nanosized materials, which is critical for predicting the stresses, interface energies, and diffusion rates within the materials. Three well-known anode NCs consisting of Sn, SnS, and SnO<sub>2</sub> were synthesized using the gas-phase laser photolysis reaction of appropriate

\* Address correspondence to  
parkjh@korea.ac.kr,  
hsk@jj.ac.kr.

Received for review September 16, 2013  
and accepted November 6, 2013.

Published online November 06, 2013  
10.1021/nn404837d

© 2013 American Chemical Society

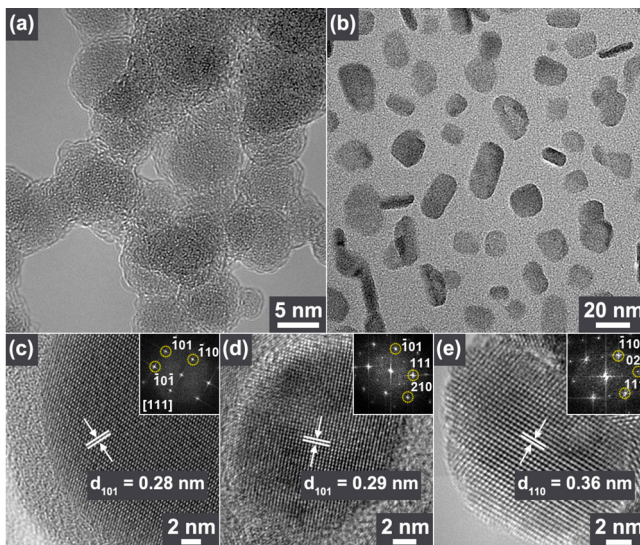


**Figure 1.** HRTEM images showing (a) spherical shapes of Sn NCs (average diameter = 7 nm) and (b) flake-like morphology of SnS NCs. Lattice-resolved and FFT images of (c) tetragonal-phase Sn ( $d_{101} = 2.8 \text{ \AA}$ ) taken at the [111] zone axis, (d) orthorhombic-phase SnS ( $d_{101} = 2.9 \text{ \AA}$ ), and (e) orthorhombic-phase SnO<sub>2</sub> ( $d_{110} = 3.6 \text{ \AA}$ ) NCs.

precursors ( $\text{Sn}(\text{CH}_3)_4$ ,  $\text{H}_2\text{S}$ ). The as-grown NCs have promise as outstanding anode materials for the development of high-performance LIBs. Our *ex situ* X-ray diffraction (XRD) and TEM analyses revealed exclusively that a diamond-type cubic-phase Sn NC was produced during the lithiation for all NCs and persisted over all cycles. *Ab initio* quantum mechanical calculations of the Li intercalation energy of cubic- and tetragonal-phase Sn were performed to explain the experimental results in terms of the thermodynamic stability and robustness of the crystal structure. To the best of our knowledge, this is the first study on the lithiation of two Sn phases using both experimental and theoretical methods.

## RESULTS AND DISCUSSION

The photolysis of  $\text{Sn}(\text{CH}_3)_4$  (tetramethyl tin, TMT) produced Sn NCs, and that of a 1:1 TMT/ $\text{H}_2\text{S}$  mixture produced SnS NCs. The SnO<sub>2</sub> NCs were synthesized by the oxidation of Sn NCs at 600–800 °C under ambient O<sub>2</sub>. The two SnO<sub>2</sub> polymorphs, metastable (at room temperature) orthorhombic (*o*-SnO<sub>2</sub>) and tetragonal rutile SnO<sub>2</sub> (*t*-SnO<sub>2</sub>), were selectively obtained by controlling the oxidation temperature.<sup>33,34</sup> XRD confirmed the structures of tetragonal-phase ( $\beta$ ) Sn (JCPDS No. 86-2265;  $a = 5.831 \text{ \AA}$ ,  $c = 3.181 \text{ \AA}$ ), orthorhombic-phase SnS (JCPDS No. 39-0354;  $a = 4.329 \text{ \AA}$ ,  $b = 11.19 \text{ \AA}$ ,  $c = 3.983 \text{ \AA}$ ), *o*-SnO<sub>2</sub> (JCPDS No. 78-1063;  $a = 4.737 \text{ \AA}$ ,  $b = 5.708 \text{ \AA}$ ,  $c = 15.865 \text{ \AA}$ ), and *t*-SnO<sub>2</sub> (JCPDS No. 77-0452;  $a = 4.755 \text{ \AA}$ ,  $c = 3.199 \text{ \AA}$ ), as shown in Figure S1 (Supporting Information). In the present work, we only used the *o*-SnO<sub>2</sub> NCs for the cycling test of LIBs.

Figure 1a shows high-resolution TEM (HRTEM) images of Sn NCs, in which their general morphology can be observed. They have a homogeneous size distribution with average diameters of 7 nm and are

usually sheathed with 1–2 nm thick C layers. We estimated the C content to be approximately 15 wt %.<sup>35</sup> The SnS NCs usually have flake-like morphologies with sizes of 10–20 nm, as shown in the HRTEM image of Figure 1b. Lattice-resolved and the corresponding fast Fourier transformed (FFT) images taken at the [111] zone axis revealed tetragonal-phase (200) fringes separated by a distance of approximately 2.9 Å, which is consistent with the value for bulk  $\beta$ -Sn (Figure 1c). It is clearly seen that the C layers sheathed the Sn NCs. The (101) fringes of the highly crystalline orthorhombic-phase SnS were separated by distances of approximately 2.9 Å, which is close to that of the bulk (Figure 1d). The single-crystalline SnO<sub>2</sub> NCs have negligible C layers after the oxidation of Sn NCs (Figure 1e). The SnO<sub>2</sub> NCs show *d*-spacing of the (110) planes of 3.6 Å, corresponding to the values for bulk orthorhombic-phase SnO<sub>2</sub>. The EDX data for individual NCs are shown in Figure S2 (Supporting Information).

We measured the discharge/charge capacities of a half-cell containing the Sn, SnS, and SnO<sub>2</sub> NCs as the active anode materials of the LIB. Figure 2a displays the charge/discharge capacity as a function of the cycle number up to 70 cycles, which was tested at a rate of 100 mA/g between 0.01 and 1.5 V. For all four materials, we conveniently defined 1 C as the theoretical capacity of pure Sn (990 mAh/g). In fact, the theoretical capacity of Sn NCs could be 900 mAh/g since the specific capacity calculated includes the C component, which makes up 15 wt % of the NCs. The theoretical 4.4 Li insertion capacity of SnS and SnO<sub>2</sub> is 780 mAh/g. The Sn, SnS, and SnO<sub>2</sub> NCs exhibited discharge capacities of 700, 880, and 540 mAh/g after 70 cycles. These values reach 78, 113, and 69% of the theoretical capacity. The Coulombic efficiency of SnS reaches an average of 98% after the first cycle, which is higher

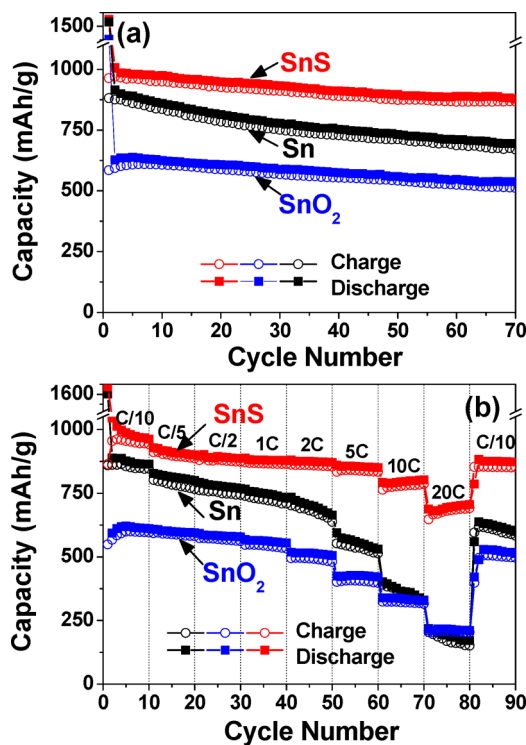


**Figure 2.** (a) Discharge/charge capacity vs cycle number for half-cells of Sn, SnS, and  $\text{SnO}_2$  NCs with a rate of 100 mAh/g ( $=\text{C}/10$ ). (b) Cycling performance as the rate is increased from  $\text{C}/10$  to 20 C.

than that of Sn and  $\text{SnO}_2$  (av. 97%). Voltage profiles and cyclic voltammetry curves are shown in Figures S3 and S4 (Supporting Information), respectively. The first discharge and charge capacities of Sn were 1580 and 880 mAh/g, respectively, with an initial Coulombic efficiency of 56%. This capacity loss can be attributed to the formation of solid electrolyte interphase (SEI) layers on the electrode surfaces during the Li storage. The first discharge and charge capacities of SnS were 1620 and 965 mAh/g, respectively, with an initial Coulombic efficiency of 60%.  $\text{SnO}_2$  shows first discharge and charge capacities of 1260 and 585 mAh/g, respectively, with an initial Coulombic efficiency of 46%. The large initial capacity losses of SnS and  $\text{SnO}_2$  could be attributed to irreversible decomposition of SnS (or  $\text{SnO}_2$ ) into Sn and  $\text{Li}_2\text{S}$  (or  $\text{Li}_2\text{O}$ ).

The rate capabilities of the different NCs were tested by sequentially measuring the capacities of Sn, SnS, and  $\text{SnO}_2$  as the charge/discharge rates increased from  $1/10$  to 20 C and then returned to  $1/10$  C, as shown in Figure 2b. As the rate is increased up to 1 C, Sn shows a small decrease in discharge capacity from 880 to 750 mAh/g. When the rate increases to 20 C, the discharge capacity decreases to 200 mAh/g. When the rate is returned back to  $1/10$  C (80–90 cycles), the discharge capacity increases to 620 mAh/g, corresponding to 70% of the initial capacity. In contrast, SnS show an extremely high rate capability: the 990 mAh/g capacity at  $1/10$  C decreases not much to 700 mAh/g at

20 C and then increases back to 875 mAh/g at  $1/10$  C after 80 cycles. The recovered capacity obtained after the return to  $1/10$  C reaches as high as 88% of the initial capacity.  $\text{SnO}_2$  shows less rate capability; the capacity was 620 mAh/g at  $1/10$  C and 220 mAh/g at 20 C. The capacity after the return to  $1/10$  C (525 mAh/g) is 85% of initial capacity. Therefore, SnS has a higher capacity as well as better rate capability than Sn and  $\text{SnO}_2$ .

*Ex situ* XRD patterns were obtained for Sn, SnS, and  $\text{SnO}_2$  electrodes before and after LIB discharge/charge cycles. Only the peaks in the range  $2\theta = 15\text{--}42^\circ$  were analyzed in order to avoid the stronger peak from the Cu foil electrode at  $2\theta = 43^\circ$ . The Sn NCs show peaks at 30.47 and 31.90° corresponding to the (200) and (101) planes of  $\beta$ -Sn (Figure 3a). The  $\beta$ -Sn peaks remain over all 70 cycles, although the intensity decreases during cycling. When the cell is discharged to 0.01 V for the first time (lithiation), new small peaks emerge (marked by the red-sashed shading) at 23.7 and 39.2°, which are matched to the (111) and (220) planes of  $\alpha$ -Sn (JCPDS No. 87-0794;  $a = 6.489$  Å). No other peaks related to the Li–Sn alloy were detected. After the cell was fully charged to 1.5 V (delithiation), the  $\alpha$ -Sn peaks disappeared. However, during the third and fifth discharging processes, the relative intensity of the  $\alpha$ -Sn peak to the  $\beta$ -Sn peak increased. These  $\alpha$ -Sn peaks persisted in the charged cell even after 70 cycles. Thus, the lithiation of  $\beta$ -Sn NCs indeed produces  $\alpha$ -Sn, which becomes a vital phase as the cycling continues.

The XRD peaks of the as-prepared SnS electrode (before the cycling test) were matched to those of orthorhombic-phase SnS (Figure 3b). The emergence of the Sn peaks during the first discharge of the cell indicates the irreversible transformation of SnS into  $\beta$ -Sn and  $\alpha$ -Sn, and which are shown by the blue- and red-sashed shading, respectively. In the cell charged for the first time, both SnS and Sn peaks coexist, indicating that not all of the SnS decomposed into Sn. The  $\beta$ -Sn peak was broader than in the case of Sn NCs, possibly because of less crystallinity due to their production from the decomposition of SnS NCs. After the third discharge, the  $\alpha$ -Sn peaks can be clearly seen, along with the main  $\beta$ -Sn peaks. The  $\alpha$ -Sn peaks became major features as the number of cycle increased, as shown in the XRD pattern of the cell after 70 cycles.

Before the cycling test, the  $\text{SnO}_2$  electrode showed peaks that exactly matched those of orthorhombic-phase  $\text{SnO}_2$  (Figures 3c). The irreversible transformation of  $\text{SnO}_2$  into  $\beta$ -Sn occurs upon the first Li insertion process. The coexistence of  $\text{SnO}_2$  and Sn peaks in the cell after the first charge indicates that the lithiation did not transform all the  $\text{SnO}_2$  into Sn. Eventually, after the third discharge, all the  $\text{SnO}_2$  was converted to  $\beta$ -Sn. A broad  $\beta$ -Sn peak was observed that was similar to that found for the SnS NCs. The production of  $\alpha$ -Sn was observed from the cells after the 10th and 70th charge

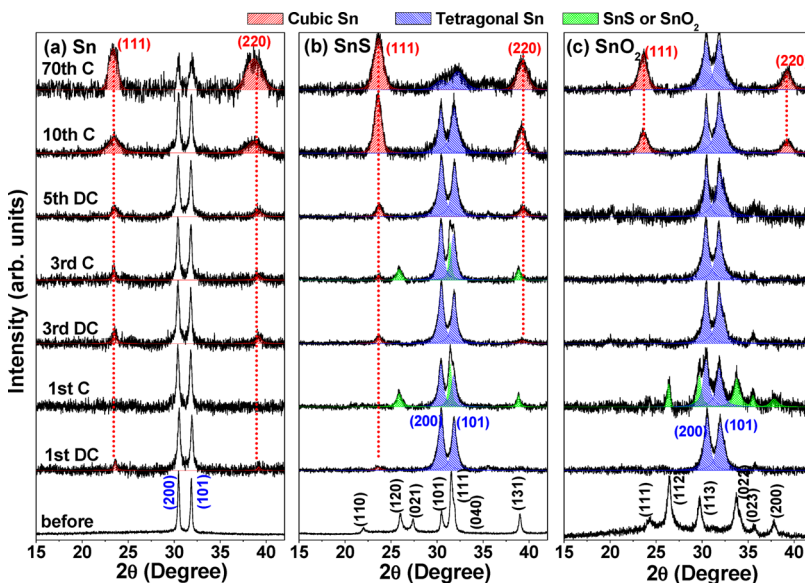


**Figure 3.** XRD pattern of (a) Sn, (b) SnS, and (c) SnO<sub>2</sub> electrodes before and after first, third, fifth, 10th, and 70th discharge (DC)/charge (C) cycles.

cycles. The peak intensity of  $\alpha$ -Sn relative to that of  $\beta$ -Sn (after the 70th charge) follows the order of SnS > Sn > SnO<sub>2</sub>, which is correlated with both their capacity and their rate capability.

A HRTEM image and its matched STEM (scanning TEM) image confirmed the crystalline nature of the Sn NCs in the fully charged SnS cell after the 70th cycle of the battery test, as shown in Figure 4a,b, respectively. The crystalline NCs (bright spots in the STEM image) are well-dispersed and embedded in the carbon/amorphous matrix. Lattice-resolved images revealed the coexistence of  $\alpha$ -Sn and  $\beta$ -Sn NCs (Figure 4c,d). The average diameter of the  $\alpha$ -Sn NCs is approximately 5 nm, which is much smaller than that of the SnS NCs. The (111) fringes are separated by a distance of approximately 3.7 Å, which corresponds to the value of bulk  $\alpha$ -Sn. The  $\beta$ -Sn NCs usually have larger diameters (average of 10 nm) than the  $\alpha$ -Sn NCs. The *d*-spacing of the (111) plane is 2.9 Å, which is close to that of  $\beta$ -Sn.

Previous *in situ* XRD studies on the lithiation and delithiation of Sn and SnO films showed evidence for a phase transformation between Sn and multiple intermediates such as Li<sub>2</sub>Sn<sub>5</sub>, LiSn, Li<sub>7</sub>Sn<sub>3</sub>, Li<sub>22</sub>Sn<sub>5</sub>, etc.<sup>36,37</sup> The Huang group reported *in situ* TEM images of a single SnO<sub>2</sub> nanowire that showed a transformation into crystalline  $\beta$ -Sn and hexagonal-phase Li<sub>13</sub>Sn<sub>5</sub> domains dispersed in an amorphous lithium oxide matrix during the initial lithiation process.<sup>38–40</sup> The lithiation accompanies a large volume expansion (250%), which is characterized by profuse dislocation plasticity. The delithiation converted the Li–Sn alloy nanoparticles back to  $\beta$ -Sn, with a much smaller volume change than that occurring during lithiation. *In situ* TEM images of lithiated SnO<sub>2</sub> nanowires consistently show that the initial Li insertion produces spherical Li<sub>x</sub>Sn nanoparticles embedded in the amorphous lithium oxide

matrix, while the wire shape remains despite the large high distortion.<sup>41,42</sup> The present result showing that the  $\beta$ -Sn phase is produced upon the lithiation of SnO<sub>2</sub> (and SnS) and that the crystalline form is maintained during the charge/discharge cycles is consistent with these previous works. The XRD peaks of Li–Sn alloys were not detected under our experimental conditions. In fact, so far, there have been no reported XRD data on the alloy formation in nanostructured anode materials.

Sn has two polymorphs at ambient pressure: a low-temperature  $\alpha$ -Sn phase (gray tin or Sn-I), which is only stable at temperatures below 13.2 °C, and a high-temperature  $\beta$ -Sn phase (white tin or Sn-II), which is stable up to 232 °C.<sup>43</sup>  $\alpha$ -Sn is a zero-band-gap semiconductor, which makes it an interesting system for studying the opening of the direct tunable band gap energy induced by the formation of alloys with cubic-phase Si or Ge.<sup>44–47</sup> The Cho group has previously reported an *ex situ* XRD pattern of  $\alpha$ -Sn produced during the electrochemical cycling of SnO<sub>2</sub> NCs.<sup>15</sup> They correlated the  $\alpha$ -Sn production with the size of cycled crystals and proposed that the cubic phase is favored at smaller sizes. Recently, Cabana and co-workers presented a TEM image of crystalline  $\alpha$ -Sn NCs produced by the delithiation of Sn NCs.<sup>12</sup> Hwang and co-workers reported calculations of the thermodynamic properties of the lithiation of  $\alpha$ -Sn, suggesting that Li insertion into  $\alpha$ -Sn is more favorable than that into the cubic-phase Si and Ge.<sup>48</sup> Kaghazchi calculated the energy barriers for the Li incorporation into the  $\alpha$ -Sn (100) surface, which are much lower than those for Li incorporation into the Si(100) surface.<sup>49</sup> However, there are no experimental works on the lithiation of  $\alpha$ -Sn to support these theoretical works yet.

To the best of our knowledge, the production of the  $\alpha$ -Sn phase by the lithiation of SnS NCs has not been

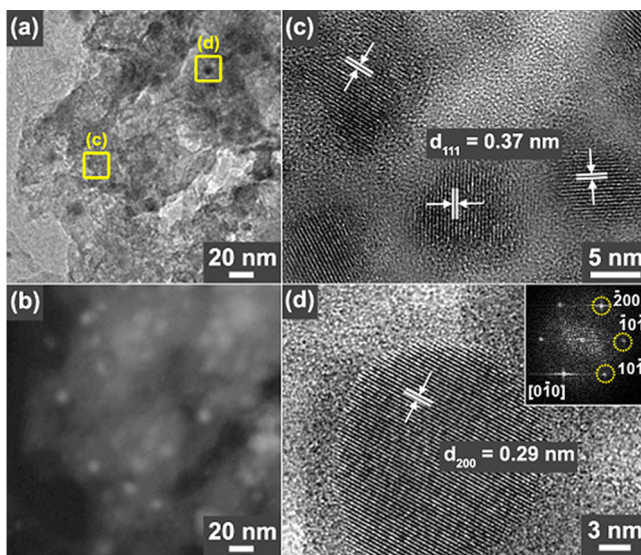


**Figure 4.** (a) HRTEM and (b) STEM images of crystalline  $\alpha$ -Sn and  $\beta$ -Sn NCs (sampled from fully charged SnS cell after 70 cycles), dispersed in carbon/amorphous matrix. Lattice-resolved images show that  $d$ -spacings of (c)  $\alpha$ -Sn (111) planes and (d)  $\beta$ -Sn (200) planes are 3.7 and 2.9 Å, respectively.

reported yet. The preferred production of the  $\beta$ -Sn phase by the irreversible transformation reaction of SnS and  $\text{SnO}_2$  would be due to its thermodynamic stability upon Li insertion, as discussed later in terms of Li intercalation energy. We found exclusively that the  $\alpha$ -Sn phase commonly emerges during the lithiation of all Sn, SnS, and  $\text{SnO}_2$  NCs and persists even after 70 cycles. The disintegration of the crystalline  $\alpha$ -Sn phase as the cycling progresses appears less significant than that of the  $\beta$ -Sn. It is expected that the maintenance of the crystalline phase increases the electrical conductivity with respect to that of the amorphous phase, leading to capacity enhancement, especially at higher discharge/charge rates. Therefore, we conclude that the production and persistence of such favorable  $\alpha$ -Sn NCs promises enhanced cycling performance.

Now, the possible reasons for the emergence of the  $\alpha$ -Sn phase have been investigated using *ab initio* calculations, as follows. Table 1 lists the parameters for the stepwise Li insertion reactions in  $\alpha$ -Sn ( $\text{Sn}_8$ ) and  $\beta$ -Sn ( $\text{Sn}_4$ ): the number of configurations considered ( $N$ ), the lattice constants ( $a = b, c$ ) of the tetragonal-phase product, the energy change for intercalation of each Li atom ( $E_b^1$ ) with respect to the energy of body-centered cubic Li, the volume per Li atom of the product ( $V^1$ ), the volume increase accompanying the Li intercalation ( $\delta V$ ), and the total energy of the most stable configuration ( $E_{\text{tot}}$ ). The stepwise Li-addition pathways in  $\alpha$ -Sn ( $\text{Sn}_8$ ) and  $\beta$ -Sn ( $\text{Sn}_4$ ) are  $\text{Sn}_8 \rightarrow \text{Sn}_8\text{Li}_2 \rightarrow \text{Sn}_8\text{Li}_3 \rightarrow \text{Sn}_8\text{Li}_4 \rightarrow \text{Sn}_8\text{Li}_5 \rightarrow \text{Sn}_8\text{Li}_6$  and  $\text{Sn}_4 \rightarrow \text{Sn}_4\text{Li}_1 \rightarrow \text{Sn}_4\text{Li}_2 \rightarrow \text{Sn}_4\text{Li}_3$ , respectively.

Figure 5 displays the most stable structures of  $\text{Sn}_8$  ( $\alpha$ -Sn),  $\text{Sn}_8\text{Li}_2$ , and  $\text{Sn}_8\text{Li}_5$  (projected onto the  $ab$  and  $ac$  planes). As a first step, five different configurations of  $\text{Sn}_8\text{Li}_2$  were considered: two diamond-type cubic

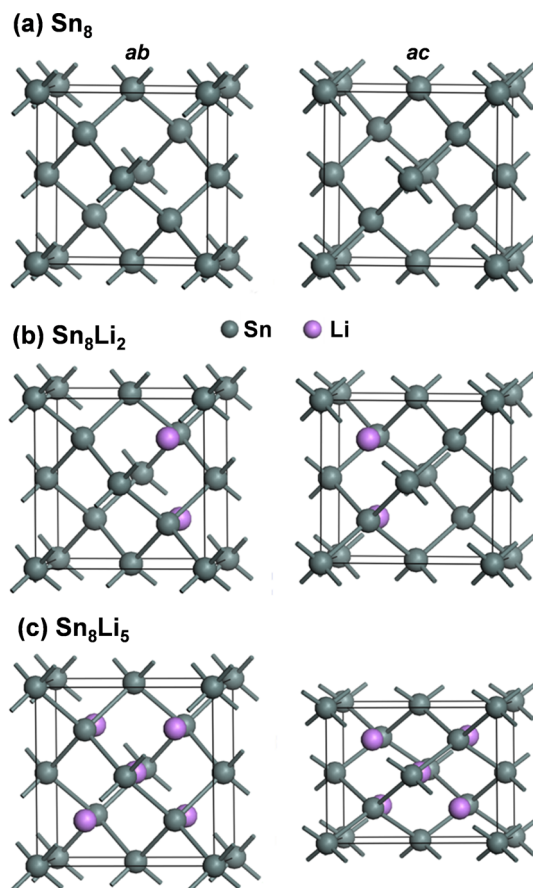


**Figure 5.** Structure of (a)  $\text{Sn}_8$  ( $\alpha$ -Sn), (b)  $\text{Sn}_8\text{Li}_2$ , and (c)  $\text{Sn}_8\text{Li}_5$ , projected onto the *ab* and *ac* planes.

configurations and three tetragonal configurations. The most stable configuration is tetragonal, where two Li atoms occupy two of the four tetrahedral sites on the (011) surface (see Figure 5a,b). Other

configurations include those in which one Li atom occupies the octahedral site at the body center of the unit cell, while the other occupies a tetrahedral site. It is highly probable that global energy minimum has been achieved since no other configuration seems to be possible. Starting from the most stable configuration of  $\text{Sn}_8\text{Li}_2$ , the stepwise Li insertions to produce  $\text{Sn}_8\text{Li}_3$ ,  $\text{Sn}_8\text{Li}_4$ ,  $\text{Sn}_8\text{Li}_5$ , and  $\text{Sn}_8\text{Li}_6$  were then studied. The crystallinity is *totally* preserved up to  $x = 5$  for  $\text{Sn}_8\text{Li}_x$  in the tetragonal phase (see Figure 5c). In short,  $\alpha$ -Sn is expected to accommodate the Li atoms up to  $\text{Sn}_8\text{Li}_5$  simply by putting them in five empty sites with little disturbance of the crystal structure. Figure S5 (Supporting Information) shows that the addition of an extra Li atom in  $\text{Sn}_8\text{Li}_6$  still preserves 81% of the crystalline Sn–Sn bonds. The  $E_b^1$  values are negative for all these processes, indicating that the Li insertions up to  $\text{Sn}_8\text{Li}_6$  are thermodynamically favorable.

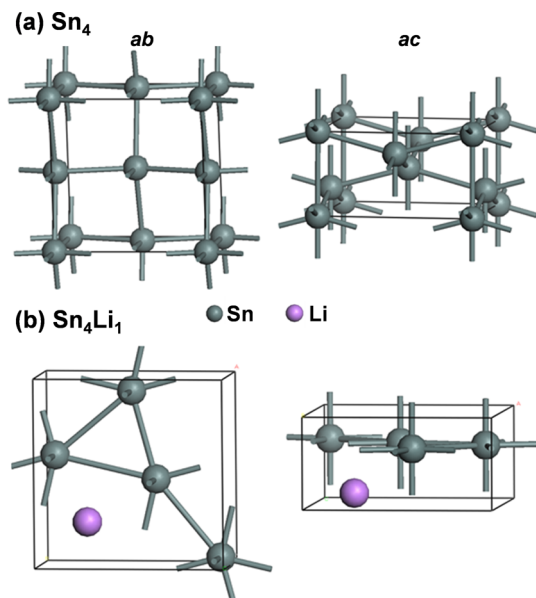


Figure 6. Structure of (a)  $\text{Sn}_4$  ( $\beta$ -Sn) and (b)  $\text{Sn}_4\text{Li}_1$ , projected onto the  $ab$  and  $ac$  planes.

Next, the Li insertion into  $\text{Sn}_4$  ( $\beta$ -Sn) was studied to determine whether the lithiated form is more stable or less stable than that of  $\text{Sn}_8$  ( $\alpha$ -Sn). The most stable configurations of  $\text{Sn}_4$  and  $\text{Sn}_4\text{Li}_1$  (projected onto the  $ab$  and  $ac$  planes) are shown in Figure 6. The Sn–Sn bonds of the  $\beta$ -Sn are almost completely broken down when one Li atom is intercalated to form  $\text{Sn}_4\text{Li}_1$ . This leads us to conjecture that  $\text{Sn}_4\text{Li}_1$  certainly becomes amorphous, which is consistent with the experimental result that  $\beta$ -Sn transforms into an amorphous phase during the repeated discharge/charge cycles. In other words,  $\beta$ -Sn is so fragile that it becomes amorphous upon the insertion of only one Li atom. Furthermore, the volume increase upon lithiation ( $\delta V = 10.7\%$ ) is larger than that ( $\delta V = 8.8\%$ ) for  $\text{Sn}_8\text{Li}_2$ , while the volume per Li atom ( $V^1$ ) is smaller ( $126.2 \text{ \AA}^3$  versus  $160.1 \text{ \AA}^3$ ). This implies that the  $\text{Li}^+–\text{Li}^+$  repulsion is more effectively released by the larger volume increase of  $\beta$ -Sn, which can be only achieved by breaking of the Sn–Sn bonds of the crystalline  $\beta$ -Sn. As a result, the Li intercalation is more favorable in the  $\beta$ -Sn, as reflected in the larger  $|E_b^1|$  value for  $\beta$ -Sn ( $=0.89 \text{ eV}$ ) than for  $\alpha$ -Sn ( $=0.40 \text{ eV}$ ). The same argument will hold for all  $x$ . It should be mentioned that the total energy of  $\text{Sn}_4\text{Li}_x$  we calculated here constitutes an upper bound to the energy of the configuration at the global energy minimum in the amorphous phase. This can be easily proven by employing larger and larger supercells in such a way that the size of supercells eventually becomes infinite, whose total energy per Sn will be certainly lower than or equal to that of the smaller supercells. In short, the true  $|E_b^1|$  value of the amorphous  $\text{Sn}_4\text{Li}_x$  is expected to be larger than the value calculated in this study (as shown in Table 1).

Figure 7 shows the total energy ( $E_{\text{tot}}$ ) of  $\text{Sn}_4\text{Li}_x$  ( $\beta$ -Sn) as a function of the Li content ( $x$ ) in comparison with  $1/2$  of the  $E_{\text{tot}}$  of  $\text{Sn}_8\text{Li}_x$  ( $\alpha$ -Sn).  $\text{Sn}_4\text{Li}_x$  is more stable than the same stoichiometric  $\text{Sn}_8\text{Li}_{2x}$  over the entire Li content range.  $\text{Sn}_4\text{Li}_1$ ,  $\text{Sn}_4\text{Li}_2$ , and  $\text{Sn}_4\text{Li}_3$  can be more stable than the  $\text{Sn}_8\text{Li}_2$ ,  $\text{Sn}_8\text{Li}_4$ , and  $\text{Sn}_8\text{Li}_6$  (at the same stoichiometry) by total energy differences of 0.33, 0.68,

TABLE 1. Parameters for the Li Intercalation Reaction of  $\alpha$ -Sn and  $\beta$ -Sn

Li intercalation reaction	$N^a$	$(a = b, c)^b$	$E_b^1 \text{ (eV)}^c$	$V^1 \text{ (\AA}^3\text{)}^d$	$\delta V \text{ (\%)}^e$	$E_{\text{tot}} \text{ (eV)}^f$
$\text{Sn}_8$ ( $\alpha$ -tin)	1	(6.65, 6.65)				$-30.685$ ( $-15.342$ ) <sup>g</sup>
$\text{Sn}_8 + 2\text{Li} \rightarrow \text{Sn}_8\text{Li}_2$ (tetragonal)	5	(6.97, 6.59)	-0.40	160.1	8.8	$-34.697$ ( $-17.349$ )
$\text{Sn}_8\text{Li}_2 + \text{Li} \rightarrow \text{Sn}_8\text{Li}_3$	3	(7.12, 6.39)	-0.57	108.0	1.2	$-36.877$ ( $-18.439$ )
$\text{Sn}_8\text{Li}_3 + \text{Li} \rightarrow \text{Sn}_8\text{Li}_4$	3	(7.34, 6.10)	-0.82	82.2	1.5	$-39.301$ ( $-19.651$ )
$\text{Sn}_8\text{Li}_4 + \text{Li} \rightarrow \text{Sn}_8\text{Li}_5$	1	(7.52, 5.95)	-0.90	67.3	2.4	$-41.812$ ( $-20.906$ )
$\text{Sn}_8\text{Li}_5 + \text{Li} \rightarrow \text{Sn}_8\text{Li}_6$	2	(7.56, 5.86)	-1.55	55.8	-0.4	$-44.973$ ( $-22.467$ )
$\text{Sn}_4$ ( $\beta$ -tin)	1	(5.95, 3.22)				-15.187
$\text{Sn}_4 + \text{Li} \rightarrow \text{Sn}_4\text{Li}_1$	4	(6.37, 3.11)	-0.89	126.2	10.7	-17.683
$\text{Sn}_4\text{Li}_1 + \text{Li} \rightarrow \text{Sn}_4\text{Li}_2$	3	(6.69, 3.21)	-1.04	71.8	13.8	-20.325
$\text{Sn}_4\text{Li}_2 + \text{Li} \rightarrow \text{Sn}_4\text{Li}_3$	3	(6.88, 3.28)	-0.92	51.8	8.0	-22.847

<sup>a</sup> Number of configurations considered. <sup>b</sup> Lattice constants ( $a = b, c$ ) in  $\text{\AA}$ . <sup>c</sup> Energy change of the Li intercalation per Li atom. <sup>d</sup> Volume per Li atom ( $V^1$ ) of the product. <sup>e</sup> Volume change accompanying the Li intercalation. <sup>f</sup> Total energy of the most stable configuration of reaction products. <sup>g</sup> The  $1/2$  value of  $E_{\text{tot}}$  for  $\text{Sn}_8\text{Li}_x$ .

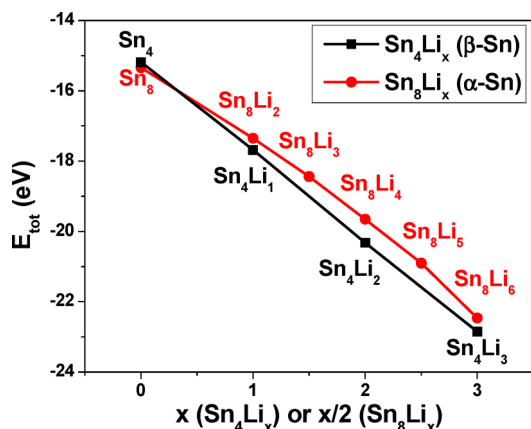


Figure 7. Total energy ( $E_{\text{tot}}$  in eV) of the  $\text{Sn}_4\text{Li}_x$  ( $\beta$ -Sn) versus  $x$ , and 1/2 of the total energy of the  $\text{Sn}_8\text{Li}_x$  ( $\alpha$ -Sn) versus  $x/2$ .

and 0.3 eV, respectively. Again, it should be noted that the  $E_{\text{tot}}$  value of  $\text{Sn}_4\text{Li}_x$  is an upper bound to the true energy, while that of the  $\text{Sn}_8\text{Li}_x$  presumably corresponds to the global energy minimum. Therefore, the relative stability of the  $\text{Sn}_4\text{Li}_x$  over the  $\text{Sn}_8\text{Li}_{2x}$  will be more pronounced than that of these calculations. The larger Li intercalation energy of the tetragonal phase than the cubic phase was also predicted for Ge.<sup>50</sup>

Our calculation shows that  $\text{Sn}_8$  is more stable than  $\text{Sn}_4$  by 0.16 eV (per  $\text{Sn}_4$ ) at 0 K. To explain why the  $\beta$ -Sn phase is favorable at room temperature, we suggest that the entropy factor compensates the small energy difference between the two phases in such a way that  $\beta$ -Sn eventually becomes more stable. It is out of the scope of this work to calculate the entropic contribution to the free energy. Nevertheless, the entropy effect could make  $\text{Sn}_4\text{Li}_x$  more stable (more negative energy) than our calculated one by an amount larger than 0.16 eV. In other words, the relative value of the free energy of  $\text{Sn}_4\text{Li}_x$  (vs  $\text{Sn}_8\text{Li}_{2x}$ ) is more negative than the difference of the  $E_{\text{tot}}$  value by at least 0.16 eV, which should make  $\text{Sn}_4\text{Li}_x$  more stable than  $\text{Sn}_8\text{Li}_{2x}$ . This assumption seems to be reasonable because the amorphous  $\text{Sn}_4\text{Li}_x$  is much more disordered than the crystalline  $\text{Sn}_8\text{Li}_{2x}$ . Therefore, at room temperature, the relative stability of  $\beta$ - $\text{Sn}_4\text{Li}_x$  could be far more pronounced if the entropy factor contributes additional stability to the amorphous  $\beta$ - $\text{Sn}_4\text{Li}_x$  phase.

Taking into account the unreached global energy minimum of the Li-intercalated  $\beta$ -Sn configuration as well as the entropy effect, we conclude that the  $\beta$ -Sn phase is thermodynamically more stable than the  $\alpha$ -Sn phase and can act a major active phase for the lithiation/delithiation processes. The lithiation of  $\beta$ -Sn changes it into an amorphous phase even at the  $\text{Sn}_4\text{Li}_1$  stoichiometry. In contrast,  $\alpha$ -Sn maintains a crystalline

form upon lithiation. Therefore, we suggest that once  $\alpha$ -Sn is produced during the lithiation process, it can retain its crystallinity over repeated cycles. The preservation of the crystalline phase could be further manifested by the comparison with the cubic-phase Ge; for example, the volume increase ( $\sim 9\%$ ) of  $\text{Sn}_8\text{Li}_2$  (from  $\text{Sn}_8$ ) is smaller than that ( $\sim 13\%$ ) in the corresponding process in  $\text{Ge}_8$ .<sup>50</sup> This observation can be understood in terms of the larger  $V^1$  value for  $\text{Sn}_8\text{Li}_2$  ( $\sim 160.1 \text{ \AA}^3$ ) than for  $\text{Ge}_8\text{Li}_2$  ( $\sim 109.7 \text{ \AA}^3$ ). The  $\text{Li}^+ - \text{Li}^+$  repulsion is weaker in the  $\text{Sn}_8$  unit cell because of the larger distances between Li atoms.

The production of  $\alpha$ -Sn could be explained by the size effect, as suggested by other research groups.<sup>12,15</sup> The lithiation process reduces the size of the NCs down to the critical size where the  $\alpha$ -Sn phase is more stable than the  $\beta$ -Sn phase. This result can be supported by our TEM images, which show that the sizes of the  $\alpha$ -Sn NCs are usually smaller than those of the  $\beta$ -Sn NCs. Another possibility is that  $\beta$ -Sn is transformed into  $\alpha$ -Sn because the Li atoms act as a catalyst. Nevertheless, further studies need to be conducted to understand the mechanism underlying the production of  $\alpha$ -Sn and its stronger tendency to be produced from SnS NCs.

## CONCLUSIONS

We synthesized Sn, SnS, and  $\text{SnO}_2$  NCs using a gas-phase laser photolysis of  $\text{Sn}(\text{CH}_3)_4$  as the Sn precursor. The gas mixture with  $\text{H}_2\text{S}$  produced SnS NCs, and the oxidation of the Sn NCs produced  $\text{SnO}_2$  NCs. The  $\beta$ -Sn (tetragonal), SnS, and  $\text{SnO}_2$  NC electrodes showed excellent cycling performance in LIBs, with capacities of 700, 880, and 540 mAh/g, respectively, after 70 cycles. The SnS NCs in particular exhibit the highest rate capabilities, 700 mAh/g at 20 C. The SnS and  $\text{SnO}_2$  NCs produced  $\beta$ -Sn NCs through an irreversible transformation. Remarkably, all three NCs produced  $\alpha$ -Sn NCs (a metastable cubic phase at room temperature) during lithiation. As the cycle number increased,  $\alpha$ -Sn became the dominant phase. A stronger tendency toward  $\alpha$ -Sn production and persistence was observed for SnS NCs, making them the best candidate for LIB anode materials.

Our first-principles calculations showed that the Li-intercalated  $\beta$ -Sn ( $\text{Sn}_4\text{Li}_x$ ,  $x = 1 - 3$ ) is thermodynamically more stable than the  $\text{Sn}_8\text{Li}_{2x}$ , assuming that the entropic contribution to the free energy further favors the  $\beta$ -Sn. Upon lithiation,  $\beta$ -Sn easily turns into an amorphous phase. In contrast,  $\alpha$ -Sn preserves its crystal structure, suggesting that once it is produced it can remain crystalline after repeated cycles. The persistence of crystalline  $\alpha$ -Sn NCs could increase the electrical conductivity of the material, leading to excellent rate capabilities.

## MATERIALS AND METHODS

Laser photolysis of tetramethyl tin (TMT, Sigma-Aldrich) or a TMT/ $\text{H}_2\text{S}$  mixture was performed using an 1064 nm Nd:YAG

pulsed laser (Coherent SL-10) operating with a repetition rate of 10 Hz and a pulse width of 10 ns. The precursors were degassed by several freeze (77 K)–pump–thaw cycles, then used without

further purification. The precursor vapors (20–50 Torr) were introduced into a 1 L volume Pyrex glass reactor, equipped with a gas valve connecting to a standard vacuum line and a 2 in. diameter quartz optical window. The laser beam was focused into the closed reactor with a 10 cm focal length lens through the optical window. The experiment was carried out using a photon energy of 0.1–0.2 J/pulse. After 1 h of laser irradiation, the gas products were vented and the freestanding NC powders (mainly formed on the reactor wall) were collected by dispersing them in ethanol, followed by evaporation and vacuum drying at room temperature. A gas mixture of TMT (20 Torr) and H<sub>2</sub>S (20 Torr) was used to synthesize the SnS NCs. The SnO<sub>2</sub> NCs were synthesized by oxidation of Sn NC at 600 or 800 °C for 30 min, under ambient O<sub>2</sub>.

The products were characterized by scanning electron microscopy (SEM, Hitachi S-4700), field-emission transmission electron microscopy (FE TEM, FEI TECNAI G2 200 kV and Jeol JEM 2100F), high-voltage transmission electron microscopy (HVEM, Jeol JEM ARM 1300S, 1.25 MV), and energy-dispersive X-ray fluorescence spectroscopy (EDX). Fast Fourier transform (FFT) images were generated by the inversion of the TEM images using Digital Micrograph GMS1.4 software (Gatan Inc.). High-resolution XRD patterns were obtained using the 9B and 3D beamlines of the Pohang Light Source (PLS) with monochromatic radiation. XRD measurement was also carried out in a Rigaku D/MAX-2500 V/PC using Cu K $\alpha$  radiation ( $\lambda = 1.54056 \text{ \AA}$ ).

For electrochemical tests, the electrodes of battery test cells were made of the active material (Sn, SnS, or SnO<sub>2</sub>), super P, and poly(acrylic acid) (PAA, 35 wt % dissolved in water; Aldrich) binder at a weight ratio of 6:2:2. The distilled water/mixed slurry was coated onto the 20  $\mu\text{m}$  thick Cu foil. The coated electrode was dried at 80 °C for 12 h and then roll-pressed. The coin-type half-cells (CR2032) were prepared in a helium-filled glovebox. The cell consisted of an electrode (containing active material), Li metal, microporous polyethylene separator, and electrolyte solution of 1 M LiPF<sub>6</sub> in 1:1:1 vol % of ethylene carbonate (EC)/ethyl methyl carbonate (EMC)/dimethyl carbonate (DMC). The performance of the cells was examined using a battery testing system (Maccor 4000) at a current density of 0.1 C to 20 C between 0.01 and 1.2 V. Cyclic voltammetry (CV) measurements were conducted (Biology SAS) using a voltage range of 0.01–2.5 V at a rate of 0.1 mV/s. For *ex situ* XRD measurements, the LIB half-cells charged or discharged to certain voltages were disassembled in a glovebox, and the electrodes were rinsed thoroughly with a DMC solution to remove the LiPF<sub>6</sub> salts.

For first-principles calculation of Li-intercalated Sn polymorphs, geometry optimizations were carried out using the Vienna ab initio simulation package (VASP).<sup>51,52</sup> Electron and ion interactions were described by the projector-augmented wave (PAW) method, which is essentially a frozen-core all-electron calculation.<sup>53</sup> The Perdew–Burke–Ernzerhof (PBE) function was adopted for the exchange-correlation function.<sup>54</sup> For structure optimization, atoms were relaxed to the direction of the Hellmann–Feynman force using the conjugate gradient method until a stringent convergence criterion (0.03 eV/Å) was satisfied. The *k*-point sampling was done using a sufficient number of points. For example, 13 × 13 × 13 *k*-points were used for the cubic (diamond) structure, for which the optimized lattice constant was 6.65 Å. When Li atoms were intercalated, the diamond phase was found to change to a tetragonal phase. The binding energy ( $E_b$ ) of Li atoms in a Sn crystal was calculated based on the chemical potential of a Li atom, which equated to its total energy in the body-centered cubic Li crystal with the optimized lattice constant. Therefore, the calculated  $E_b$  corresponds to the lower bound of the real binding energy, and the real binding energy will be larger than  $|E_b|$  in magnitude.

**Conflict of Interest:** The authors declare no competing financial interest.

**Acknowledgment.** This study was supported by NRF (2011-001-5235; 2011-002-0090; 2012-R1A1A-2039084) and WCU (R31-2012-000-10035-0). The HVEM (Daejeon) and XPS (Pusan) measurements were performed at the KBSI. The experiments at the PLS were partially supported by MOST and POSTECH. Computations

were performed using a supercomputer at the Korea Institute of Science and Technology Information (KSC-2013-C2-014).

**Supporting Information Available:** XRD, EDX, charge and discharge voltage profiles, and cyclic voltammetry data. This material is available free of charge via the Internet at <http://pubs.acs.org>.

## REFERENCES AND NOTES

- Hansen, M. *Constitution of Binary Alloys*; Genium: Schenectady, NY, 1989.
- Huggins, R. A. Lithium Alloy Negative Electrodes. *J. Power Sources* **1999**, *81*–82, 13–19.
- Winter, M.; Besenhard, J. O. Electrochemical Lithiation of Tin and Tin-Based Intermetallics and Composites. *Electrochim. Acta* **1999**, *45*, 31–50.
- Lee, K. T.; Jung, Y. S.; Oh, S. M. Synthesis of Tin-Encapsulated Spherical Hollow Carbon for Anode Material in Lithium Secondary Batteries. *J. Am. Chem. Soc.* **2003**, *125*, 5652–5653.
- Noh, M.; Kwon, Y.; Lee, H.; Cho, J.; Kim, Y.; Kim, M. G. Amorphous Carbon-Coated Tin Anode Material for Lithium Secondary Battery. *Chem. Mater.* **2005**, *17*, 1926–1929.
- Derrien, G.; Hassoun, J.; Panero, S.; Scrosati, B. Nanostructured Sn–C Composite as an Advanced Anode Material in High-Performance Lithium-Ion Batteries. *Adv. Mater.* **2007**, *19*, 2336–2340.
- Zhang, W.-M.; Hu, J.-S.; Guo, Y.-G.; Zheng, S.-F.; Zhong, L.-S.; Song, W.-G.; Wan, L.-J. Tin-Nanoparticles Encapsulated in Elastic Hollow Carbon Spheres for High-Performance Anode Material in Lithium-Ion Batteries. *Adv. Mater.* **2008**, *20*, 1160–1165.
- Hassoun, J.; Derrien, G.; Panero, S.; Scrosati, B. A. Nanostructured Sn–C Composite Lithium Battery Electrode with Unique Stability and High Electrochemical Performance. *Adv. Mater.* **2008**, *20*, 3169–3175.
- Yu, Y.; Gu, L.; Wang, C.; Dhanabalan, A.; van Aken, P. A.; Maier, J. Encapsulation of Sn@Carbon Nanoparticles in Bamboo-like Hollow Carbon Nanofibers as an Anode Material in Lithium-Based Batteries. *Angew. Chem., Int. Ed.* **2009**, *48*, 6485–6489.
- Luo, B.; Wang, B.; Liang, M.; Ning, J.; Li, X.; Zhi, L. Reduced Graphene Oxide-Mediated Growth of Uniform Tin-Core/Carbon-Sheath Coaxial Nanocables with Enhanced Lithium Ion Storage Properties. *Adv. Mater.* **2012**, *24*, 1405–1409.
- Xu, Y.; Liu, Q.; Zhu, Y.; Liu, Y.; Langrock, A.; Zachariah, M. R.; Wang, C. Uniform Nano-Sn/C Composite Anodes for Lithium Ion Batteries. *Nano Lett.* **2013**, *13*, 470–474.
- Xu, L.; Kim, C.; Shukla, A. K.; Dong, A.; Mattox, T. M.; Milliron, D. J.; Cabana, J. Monodisperse Sn Nanocrystals as a Platform for the Study of Mechanical Damage during Electrochemical Reactions with Li. *Nano Lett.* **2013**, *13*, 1800–1805.
- Idota, Y.; Kubota, T.; Matsufuji, A.; Maekawa, Y.; Miyasaka, T. Tin-Based Amorphous Oxide: A High-Capacity Lithium-Ion–Storage Material. *Science* **1997**, *276*, 1395–1397.
- Fan, J.; Wang, T.; Yu, C.; Tu, B.; Jiang, Z.; Zhao, D. Ordered, Nanostructured Tin-Based Oxides/Carbon Composite as the Negative-Electrode Material for Lithium-Ion Batteries. *Adv. Mater.* **2004**, *16*, 1432–1436.
- Kim, C.; Noh, M.; Choi, M.; Cho, J.; Park, B. Critical Size of a Nano SnO<sub>2</sub> Electrode for Li-Secondary Battery. *Chem. Mater.* **2005**, *17*, 3297–3301.
- Park, M.-S.; Wang, G.-X.; Kang, Y.-M.; Wexler, D.; Dou, S.-X.; Liu, H.-K. Preparation and Electrochemical Properties of SnO<sub>2</sub> Nanowires for Application in Lithium-Ion Batteries. *Angew. Chem., Int. Ed.* **2007**, *46*, 750–753.
- Paek, S.-M.; Yoo, E.; Honma, I. Enhanced Cyclic Performance and Lithium Storage Capacity of SnO<sub>2</sub>/Graphene Nanoporous Electrodes with Three-Dimensionally Delaminated Flexible Structure. *Nano Lett.* **2009**, *9*, 72–75.
- Li, X.; Meng, X.; Liu, J.; Geng, D.; Zhang, Y.; Banis, M. N.; Li, Y.; Yang, J.; Li, R.; Sun, X.; et al. Tin Oxide with Controlled Morphology and Crystallinity by Atomic Layer Deposition

- onto Graphene Nanosheets for Enhanced Lithium Storage. *Adv. Funct. Mater.* **2012**, *22*, 1647–1654.
19. Kravchyk, K.; Protesescu, L.; Bodnarchuk, M. I.; Krumeich, F.; Yarema, M.; Walter, M.; Guntlin, C.; Kovalenko, M. V. Monodisperse and Inorganically Capped Sn and Sn/SnO<sub>2</sub> Nanocrystals for High-Performance Li-Ion Battery Anodes. *J. Am. Chem. Soc.* **2013**, *135*, 4199–4202.
20. Wang, L.; Wang, D.; Dong, Z.; Zhang, F.; Jin, J. Interface Chemistry Engineering for Stable Cycling of Reduced GO/SnO<sub>2</sub> Nanocomposites for Lithium Ion Battery. *Nano Lett.* **2013**, *13*, 1711–1716.
21. Hong, Y. J.; Son, M. Y.; Kang, Y. C. One-Pot Facile Synthesis of Double-Shelled SnO<sub>2</sub> Yolk-Shell-Structured Powders by Continuous Process as Anode Materials for Li-Ion Batteries. *Adv. Mater.* **2013**, *25*, 2279–2283.
22. Prabakar, S. J. R.; Hwang, Y.-H.; Bae, E.-G.; Shim, S.; Kim, D.; Lah, M. S.; Sohn, K.-S.; Pyo, M. SnO<sub>2</sub>/Graphene Composites with Self-Assembled Alternating Oxide and Amine Layers for High Li-Storage and Excellent Stability. *Adv. Mater.* **2013**, *25*, 3307–3312.
23. Kim, T.-J.; Kim, C.; Son, D.; Choi, M.; Park, B. Novel SnS<sub>2</sub>-Nanosheet Anodes for Lithium-Ion Batteries. *J. Power Sources* **2007**, *167*, 529–535.
24. Seo, J.-W.; Jang, J.-T.; Park, S.-W.; Kim, C.; Park, B.; Cheon, J. Two-Dimensional SnS<sub>2</sub> Nanoplates with Extraordinary High Discharge Capacity for Lithium Ion Batteries. *Adv. Mater.* **2008**, *20*, 4269–4273.
25. Zai, J.; Wang, K.; Su, Y.; Qian, X.; Chen, J. High Stability and Superior Rate Capability of Three-Dimensional Hierarchical SnS<sub>2</sub> Microspheres as Anode Material in Lithium Ion Batteries. *J. Power Sources* **2011**, *196*, 3650–3654.
26. Zhang, Y.; Lu, J.; Shen, S.; Xu, H.; Wang, Q. Ultralarge Single Crystal SnS Rectangular Nanosheets. *Chem. Commun.* **2011**, *47*, 5226–5228.
27. Vaughn, D. D.; Hentz, O. D.; Chen, S.; Wang, D.; Schaa, R. E. Formation of SnS Nanoflowers for Lithium Ion Batteries. *Chem. Commun.* **2012**, *48*, 5608–5610.
28. Jiang, Z.; Wang, C.; Du, G.; Zhong, Y. J.; Jiang, J. Z. *In Situ* Synthesis of SnS<sub>2</sub>@Graphene Nanocomposites for Rechargeable Lithium Batteries. *J. Mater. Chem.* **2012**, *22*, 9494–9496.
29. Zhang, M.; Lei, D.; Yu, X.; Chen, L.; Li, Q.; Wang, Y.; Wang, T.; Cao, G. Graphene Oxide Oxidizes Stannous Ions To Synthesize Tin Sulfide—Graphene Nanocomposites with Small Crystal Size for High Performance Lithium Ion Batteries. *J. Mater. Chem.* **2012**, *22*, 23091–23097.
30. Yin, J.; Cao, H.; Zhou, Z.; Zhang, J.; Qu, M. SnS<sub>2</sub>@Reduced Graphene Oxide Nanocomposites as Anode Materials with High Capacity for Rechargeable Lithium Ion Batteries. *J. Mater. Chem.* **2012**, *22*, 23963–23970.
31. Sathish, M.; Mitani, S.; Tomai, T.; Honma, I. Ultrathin SnS<sub>2</sub> Nanoparticles on Graphene Nanosheets: Synthesis, Characterization, and Li-Ion Storage Applications. *J. Phys. Chem. C* **2012**, *116*, 12475–12481.
32. Du, Y.; Yin, Z.; Rui, X.; Zeng, Z.; Wu, X.-J.; Liu, J.; Zhu, Y.; Zhu, J.; Huang, X.; Yan, Q.; et al. A Facile, Relative Green, and Inexpensive Synthetic Approach toward Large-Scale Production of SnS<sub>2</sub> Nanoplates for High-Performance Lithium-Ion Batteries. *Nanoscale* **2013**, *5*, 1456–1459.
33. Haines, J.; Leger, J. M. X-ray Diffraction Study of the Phase Transitions and Structural Evolution of Tin Dioxide at High Pressure: Relationships between Structure Types and Implications for Other Rutile-Type Dioxides. *Phys. Rev. B* **1997**, *55*, 11144–11154.
34. Shek, C. H.; Lai, J. K. L.; Lin, G. M.; Zheng, Y. F.; Liu, W. H. Nanomicrostructure, Chemical Stability and Abnormal Transformation in Ultrafine Particles of Oxidized Tin. *J. Phys. Chem. Solids* **1997**, *58*, 13–17.
35. Cho, Y. J.; Kim, C. H.; Im, H. S.; Myung, Y.; Kim, H. S.; Back, S. H.; Lim, Y. R.; Jung, C. S.; Jang, D. M.; Park, J.; et al. Germanium–Tin Alloy Nanocrystals for High-Performance Lithium Ion Batteries. *Phys. Chem. Chem. Phys.* **2013**, *15*, 11691–11695.
36. Rhodes, K. J.; Meisner, R.; Kirkham, M.; Dudney, N.; Daniel, C. *In Situ* XRD of Thin Film Tin Electrodes for Lithium Ion Batteries. *J. Electrochem. Soc.* **2012**, *159*, A294–A299.
37. Courtney, I. A.; Dahn, J. R. Electrochemical and *In Situ* X-ray Diffraction Studies of the Reaction of Lithium with Tin Oxide Composites. *J. Electrochem. Soc.* **1997**, *144*, 2045–2052.
38. Huang, J. Y.; Zhong, L.; Wang, C. M.; Sullivan, J. P.; Xu, W.; Zhang, L. Q.; Mao, S. X.; Hudak, N. S.; Liu, X. H.; Subramanian, A.; et al. *In Situ* Observation of the Electrochemical Lithiation of a Single SnO<sub>2</sub> Nanowire Electrode. *Science* **2010**, *330*, 1515–1520.
39. Zhang, L. Q.; Liu, X. H.; Liu, Y.; Huang, S.; Zhu, T.; Gui, L.; Mao, S. X.; Ye, Z. Z.; Wang, C. M.; Sullivan, J. P.; et al. Controlling the Lithiation-Induced Strain and Charging Rate in Nanowire Electrodes by Coating. *ACS Nano* **2011**, *5*, 4800–4809.
40. Liu, X. H.; Liu, Y.; Kushima, A.; Zhang, S.; Zhu, T.; Li, J.; Huang, J. Y. *In Situ* TEM Experiments of Electrochemical Lithiation and Delithiation of Individual Nanostructures. *Adv. Energy Mater.* **2012**, *2*, 722–741.
41. Wang, C.-M.; Xu, W.; Liu, J.; Zhang, J. G.; Saraf, L. V.; Arey, B. W.; Choi, D.; Yang, Z. G.; Xiao, J.; Thevuthasan, S.; et al. *In Situ* Transmission Electron Microscopy Observation of Microstructure and Phase Evolution in a SnO<sub>2</sub> Nanowire during Lithium Intercalation. *Nano Lett.* **2011**, *11*, 1874–1880.
42. Nie, A.; Gan, L.-Y.; Cheng, Y.; Asayesh-Ardakani, H.; Li, Q.; Dong, C.; Tao, R.; Mashayek, F.; Wang, H.-T.; Schwingenschlögl, U.; et al. Atomic-Scale Observation of Lithiation Reaction Front in Nanoscale SnO<sub>2</sub> Materials. *ACS Nano* **2013**, *7*, 6203–6211.
43. Donohue, J. *The Structures of the Elements*; Wiley: New York, 1974.
44. Groves, S.; Paul, W. Band Structure of Gray Tin. *Phys. Rev. Lett.* **1963**, *11*, 194–196.
45. He, G.; Atwater, H. A. Interband Transitions in Sn<sub>x</sub>Ge<sub>1-x</sub> Alloys. *Phys. Rev. Lett.* **1997**, *79*, 1937–1940.
46. Bauer, M.; Taraci, J.; Tolle, J.; Chizmeshya, A. V. G.; Zollner, S.; Smith, D. J.; Menendez, J.; Hu, C.; Kouvetsakis, J. Ge–Sn Semiconductors for Band-Gap and Lattice Engineering. *Appl. Phys. Lett.* **2002**, *81*, 2992–2994.
47. Lin, H.; Chen, R.; Lu, W.; Huo, Y.; Kamins, T. I.; Harris, J. S. Structural and Optical Characterization of Si<sub>x</sub>Ge<sub>1-x-y</sub>Sn<sub>y</sub> Alloys Grown by Molecular Beam Epitaxy. *Appl. Phys. Lett.* **2012**, *100*, 141908.
48. Chou, C.-Y.; Kim, H.; Hwang, G. S. A Comparative First-Principles Study of the Structure, Energetics, and Properties of Li-M (M = Si, Ge, Sn) Alloys. *J. Phys. Chem. C* **2011**, *115*, 20018–20026.
49. Kaghazchi, P. Theoretical Studies of Lithium Incorporation into  $\alpha$ -Sn(100). *J. Chem. Phys.* **2013**, *138*, 054706.
50. Cho, Y. J.; Im, H. S.; Kim, H. S.; Myung, Y.; Back, S. H.; Lim, Y. R.; Jung, C. S.; Jang, D. M.; Park, J.; Cha, E. H.; et al. Tetragonal Phase Germanium Nanocrystals in Lithium Ion Batteries. *ACS Nano* **2013**, *7*, 9075–9084.
51. Kresse, G.; Hafner, J. *Ab Initio* Molecular Dynamics for Liquid Metals. *Phys. Rev. B* **1993**, *47*, 558.
52. Kresse, G.; Furthmüller, J. Efficient Iterative Schemes for *Ab Initio* Total-Energy Calculations Using a Plane-Wave Basis Set. *Phys. Rev. B* **1996**, *54*, 11169.
53. Kresse, G.; Joubert, D. From Ultrasoft Pseudopotentials to the Projector Augmented-Wave Method. *Phys. Rev. B* **1999**, *59*, 1758–1775.
54. Perdew, J. P.; Burke, K.; Ernzerhof, M. Generalized Gradient Approximation Made Simple. *Phys. Rev. Lett.* **1996**, *77*, 3865–3868.